



# Geodetic imaging of thermal deformation in geothermal reservoirs - production, depletion and fault reactivation



Kyungjae Im<sup>a,\*</sup>, Derek Elsworth<sup>a</sup>, Yves Guglielmi<sup>b</sup>, Glen S. Mattioli<sup>c,d</sup>

<sup>a</sup> Department of Energy and Mineral Engineering, EMS Energy Institute, and G3 Center, The Pennsylvania State University, University Park, PA 16802, United States

<sup>b</sup> Lawrence Berkeley National Laboratory, Berkeley, CA 94720, United States

<sup>c</sup> Department of Earth and Environmental Sciences, University of Texas at Arlington, Arlington, TX 76019 United States

<sup>d</sup> UNAVCO Inc., Boulder, CO 80301, United States

## ARTICLE INFO

### Article history:

Received 21 September 2016

Received in revised form 14 March 2017

Accepted 20 March 2017

Available online 22 March 2017

### Keywords:

Geothermal

Surface deformation

Induced microearthquakes

Geodesy

Permeability

## ABSTRACT

We investigate thermally induced surface deformation in geothermal systems. To define source mechanisms at depth, we assess the mechanical process of subsurface deformation by assuming a spherically cooled fractured reservoir in an infinite medium and derive relations that define magnitudes of thermal contraction, stress change and permeability evolution. The magnitude of thermal deformation in typical geothermal system is larger than anticipated and suggests two different modalities of surface subsidence – thermal contraction and fault reactivation. Here, surface deformation (vertical displacement, surface tilt and horizontal strain) induced by the two different modalities are assessed with Mogi (contraction) and Okada (slip) models and compared with instrumental sensitivity of high precision surface geodetic tools. We show that 1 year of geothermal operation at 10 MW with a power plant conversion efficiency of 12% can yield  $\sim 3.0 \times 10^4 \text{ m}^3$  of subsurface volume change. For a reservoir at 2000 m depth, this induces  $\sim 1.7 \text{ mm}$  of vertical surface displacement,  $\sim 800$  nano-radians of surface tilt and  $\sim 900$  nano-strains of surface strain. This result implies that typically observed magnitudes of surface subsidence (order of cm/year) are naturally expected in massive (100 MW scale) geothermal operations and observed surface subsidence may largely be the result of thermal contraction. Conversely, thermal unloading can trigger fault reactivation. Analysis with an Okada slip model shows these shear offsets on pre-existing faults can also result in surface deformations of considerable magnitude. Our analysis of field operational data from various geothermal projects suggests that both thermal contraction and slow fault reactivation may contribute to the observed large surface deformation. Comparison of predicted deformation with instrumental sensitivity of high precision surface tools confirms that geodetic signals, especially tilt and strain, are indeed sufficiently large to describe reservoir evolution and to potentially deconvolve reservoir parameters of interest, such as permeability.

© 2017 Elsevier B.V. All rights reserved.

## 1. Introduction

Surface deformations of significant magnitude in a number of geothermal fields have been observed by both interferometric methods (InSAR) (Ali et al., 2016; Eneva et al., 2012; Falorni et al., 2011; Fialko and Simons, 2000; Foxall and Vasco, 2003; Vasco et al., 2002b; Vasco et al., 2013) and by direct measurement of surface tilt (Vasco et al., 2002a). Subsurface deformation induced by cold water injection generally conforms to two different modalities: (i) isotropic volume change and (ii) injection induced shear offset on finite faults. Isotropic volume change can be induced by either thermal contraction (volume decrease) or pressure dilation (volume increase) in the reservoir with shear slip similarly resulting from changes in effective stress induced by changes

in fluid pressures or temperature. Ali et al. (2016) recently show that surface subsidence in the Brady Hot Springs geothermal field may result from the contraction of shallow strata similar to the potential for pressure driven early-time slip and temperature driven late-time slip postulated to result in geothermal reservoirs (Gan and Elsworth, 2014).

Although surface deformation in geothermal systems can be induced by both pressure and temperature change, observations suggest that it may be mainly temperature driven since the deformations are slow and continuous – similar to the progress of conduction-limited heat transport. Surface subsidence rates are typically several cm/year and continuous through geothermal operations. As discussed by Gan and Elsworth (2014), temperature driven stress change is slow and continues until the reservoir is thermally depleted. Conversely, pressure change is concentrated early during fluid injection, limited by boundaries (well bore pressures) and typically localized near-wellbore regions of injection or production, where effects are most focused.

\* Corresponding author.

E-mail address: [kxi123@psu.edu](mailto:kxi123@psu.edu) (K. Im).

Linking the observed deformation with a subsurface mechanism helps define active processes during reservoir evolution. Such models may be used to constrain magnitudes of heat energy transfer from rock to fluid and the evolution of transport characteristics of the reservoir. The detection of slip processes on finite faults in turn constrains fluid flow and the evolution of major flow paths, and may allow the precursors to injection-induced seismicity to be defined and monitored.

State of the art instruments that measure strain and tilt provide extremely high sensitivity and resolution of surface deformation. The Gladwin tensor strainmeter (GTSM) provides a precision of <1 nano-strain in the short term (Gladwin, 1984) and current commercial tilt meters (Pinnacle Denali tiltmeter) have a sensitivity ~1 nano-radian (Wright et al., 1998). We will demonstrate below that these instruments have sensitivities (in this study, 1 nano-radian and 1 nano-strain) that are sufficiently fine to describe reservoir thermal processes, and thus will provide valuable information on reservoir evolution and improve geothermal development practices in the field.

Below, we first assess mechanisms of thermally-driven contraction, stress change and permeability evolution of a fractured reservoir within an elastic half-space. This then defines the magnitudes of the signal, considering the coupling and decoupling processes between the reservoir and the surrounding rock. We then define the expected surface deformation induced by both thermal contraction and field scale fault reactivation using the Mogi volumetric model (Mogi, 1958) and the Okada shear slip model (Okada, 1985). These are then compared with instrumental resolutions of current geodetic methods. Further, we analyze existing surface deformation data using these models to deconvolve processes within deep reservoirs.

## 2. Surface deformation

We assess surface deformation developed by two modes of subsurface deformations: (i) volume change due to thermal contraction and (ii) shear deformation due to slip on a finite fault plane. We apply the Mogi (1958) solution to analyze volume change and the Okada (1985) solution for shear deformation offset at depth to estimate the magnitude of maximum deformations: vertical displacement, surface tilt and strain.

### 2.1. Volume change

Volumetric strain,  $\varepsilon_v$ , induced by temperature change of unconstrained media is

$$\varepsilon_v = \alpha_v \Delta T \quad (1)$$

where,  $\alpha_v$  is volumetric thermal expansion coefficient and  $\Delta T$  is temperature change. Experimental data indicate that the volumetric thermal expansion coefficient of igneous rock is generally within the range  $2 \times 10^{-5}$ – $7 \times 10^{-5}$  within the temperature range between 30 °C and 400 °C (Cooper and Simmons, 1977). The magnitude of the thermal expansion coefficient suggests that thermal stresses can surpass poroelastic stresses in general geothermal system after sufficient duration of injection/recovery. For example, a temperature change of 100 °C with  $\alpha_v = 5 \times 10^{-5}$  induces a volumetric strain of 0.005 while a 20 MPa change in pressure with a bulk modulus of 20 GPa induces only a volumetric strain of 0.001 in an unconfined system.

#### 2.1.1. Coupled deformation

Eq. (1) assumes strain under invariant stress. The presence of the surrounding rock, however, reduces the magnitude of deformation. The deformation reduction for elastically confined deformation of the ellipsoidal inclusion in an infinite elastic medium is solved analytically by Eshelby (1957). In the solution, volumetric strain of the unconstrained body  $\varepsilon^*$  is defined by the relation

$$\varepsilon_{ij}^c = S_{ijkl} \varepsilon_{kl}^* \quad (2)$$

where  $\varepsilon^c$  is the strain in the confined inclusion and  $S_{ijkl}$  is the Eshelby tensor that is dependent on the shape of the inclusion. The relation can be directly applied to the constrained thermal contraction by substituting  $\varepsilon_{ii}^* = 1/3\alpha_v \Delta T$  and  $\varepsilon_{ij}^* = \varepsilon_{jk}^* = \varepsilon_{ki}^* = 0$ . The Eshelby solution is derived by removing, then deforming and re-emplacing the ellipsoidal inclusion. Using a similar approach, we analyze a spherical fractured reservoir that has a modulus different from that of the surrounding rock (spherical soft inclusion) by assuming that all heat sources come from this localized volume. The Young's modulus of the fractured reservoir can be expressed as (Goodman, 1980),

$$\frac{1}{E_{res}} = \frac{1}{E} + \frac{1}{k_n S} \quad (3)$$

where,  $k_n$  is normal stiffness of an individual fracture and  $S$  is fracture spacing and  $E$  is intact rock's Young's modulus. Accordingly, the fractured rock will generally be less stiff than the intact rock.

Fig. 1 illustrates deformations due to pressure change within (i) a spherical reservoir under zero stress, (ii) a spherical cavity in an infinite medium and (iii) their coupled behavior. We assume that the modulus of host and reservoir are different but that each are uniform and homogeneous. The magnitude of the coupled strain can be recovered as follows. Volumetric strain induced by pressure change in the unconstrained sphere (reservoir) with bulk modulus  $K_{res}$  (Fig. 1 (a)) is

$$\varepsilon_{v,sphere} = \frac{\Delta P_{sphere}}{K_{res}} \quad (4)$$

For a spherical cavity in a matrix with shear modulus  $G$ , radial displacement ( $u_r$ ) at the cavity boundary  $r$  with an internal pressure change  $\Delta P$ , the deformation is  $u_r = \Delta P \cdot r / 4G$  [Yu and Housby, 1991]. Using this, volumetric strain induced by the pressure change in the spherical cavity in an infinite body (host rock) with shear modulus  $G_{host}$  (Fig. 1 (b)) can be calculated as,

$$\varepsilon_{v,cavity} = \frac{\Delta P_{cavity}}{\frac{4G_{host}}{3}} \quad (5)$$

Note that the modulus of the reservoir ( $K_{res}$ ) and the host rock ( $G_{host}$ ) are different, but each medium is assumed to be a uniform elastic material. If the sphere is embedded in the cavity and both sphere and cavity deform together with the same pressure change in the sphere, then the deformations of both sphere and cavity will be the same, with the same volumetric strain (boundary displacements linked) as,

$$\varepsilon_v = \varepsilon_{v,sphere} = \varepsilon_{v,cavity} \quad (6)$$

and the total pressure change used to deform both sphere and cavity is the sum of the applied pressures that induces the strain in both sphere and cavity,

$$\Delta P = \Delta P_{sphere} + \Delta P_{cavity} \quad (7)$$

Eqs. (4), (5), (6) and (7) yield volumetric strain of coupled deformation as (Fig. 1 (c)),

$$\varepsilon_v = \frac{\Delta P}{K_{res} + \frac{4G_{host}}{3}} \quad (8)$$

The equivalent pressure due to the thermal stress can be calculated by equating Eqs. (1) and (4),

$$\Delta P = K_{res} \alpha_v \Delta T \quad (9)$$

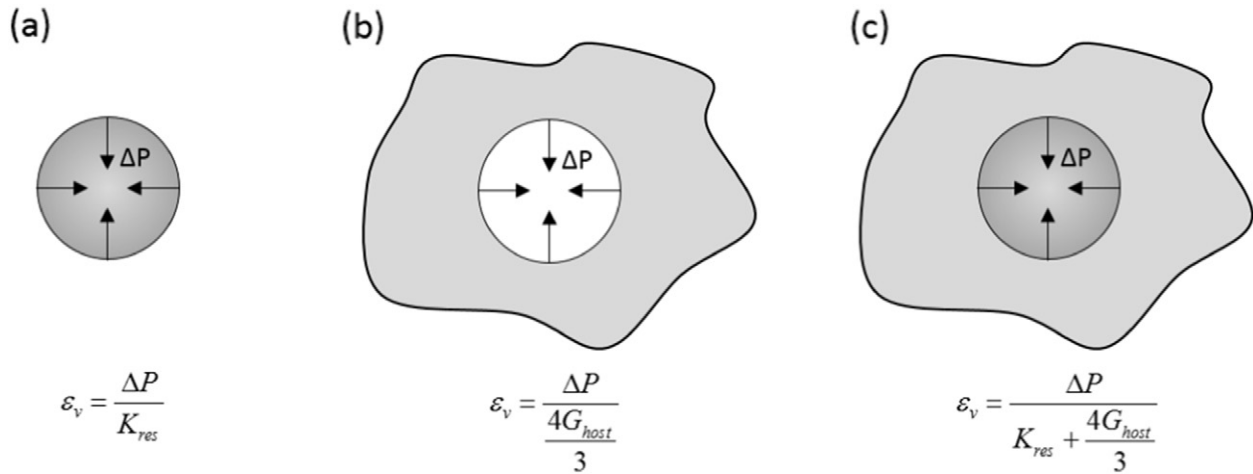


**Fig. 1.** Volumetric strain induced by pressure change,  $\Delta P$ , of (a) zero stress (no surroundings) sphere with bulk modulus  $K_{res}$ , and, (b) spherical cavity in an infinite body with shear modulus  $G_{host}$ . When the sphere and cavity deform with the same volumetric strain, the volumetric modulus of the coupled deformation (c) becomes the sum of bulk modulus of (a) and (b),  $K_{res} + 4G_{host}/3$ .

Substituting Eqs. (9) into (8) yields

$$\varepsilon_v = \frac{1}{1 + \frac{4G_{host}}{3K_{res}}} \alpha_v \Delta T \quad (10)$$

or,

$$\varepsilon_v = \frac{1}{1 + \frac{2(1-2\nu)E_{host}}{(1+\nu)E_{res}}} \alpha_v \Delta T \quad (11)$$

where,  $\nu$  is Poisson's ratio and  $E_{host}$  and  $E_{res}$  are the Young's modulus of the host rock and reservoir rock, respectively. We note that the result is identical to that of an Eshelby spherical inclusion when  $E_{host} = E_{res}$ . Although this work focuses on a spherical cooled (mature) reservoir, the correspondence between Eq. (11) and that for an Eshelby inclusion indicates that the solution can be extended to an arbitrarily shaped ellipsoid.

Eq. (11) indicates that the stress/strain change inside of a uniformly cooled sphere in an infinite medium is also uniform and this is independent of the form of the external temperature field. Imagine a sphere that is cooled by  $\Delta T$  and sustains a volumetric strain of  $\varepsilon_v$ . If a concentric inner sphere inside this outer sphere is cooled by an additional  $\Delta T$  then Eq. (11) (and the Eshelby solution) defines the induced strain in the inner sphere simply as  $2\varepsilon_v$ , which is identical to the case of a single sphere cooled by  $2\Delta T$  without outer sphere. This result reveals that the existence of an outer sphere does not affect the stress/strain field of an embedded inner sphere. Thus, the thermal gradient in the outer shell does not affect the stress/strain field inside the embedded uniformly cooled sphere if the moduli are independent of temperature and the thermal gradient is also radially symmetric. This observation significantly simplifies the stress/strain field and the resulting evaluation of permeability evolution.

Since  $\alpha_v \Delta T$  is the unconstrained volumetric strain (Eq. (1)), the multipliers on  $\alpha_v \Delta T$  in Eqs. (10) and (11) indicate the ratio of deformation reduction resulting from the existence of the surrounding rock. Since the elastic modulus of the fractured rock is generally smaller than that for unfractured rock (Eq. (3)), the reduction ratio is maximum when  $E_{host} = E_{res}$ . For example, when  $E_{host} = E_{res}$  and Poisson's ratio 0.25, the deformation ratio is 0.56. That is, the constrained volumetric strain magnitude arising from thermal expansion (or contraction) would be reduced to 56% of the zero stress case.

### 2.1.2. Decoupling between reservoir and host

The reduction of thermal contraction rate in coupled deformation (difference between Eq. (1) and Eq. (11)) indicates that the stress that resists thermal contraction would be induced in the reservoir. Thermal contraction will reduce the applied in situ stress in the reservoir and may eventually induce extensional stress. When the net stress of the reservoir becomes extensional and if the reservoir is highly fractured, further thermal contraction would open internal existing fractures rather than pulling-in the surrounding rock. Accordingly, the deformation of the reservoir and the surrounding rock decouples and Eq. (6) is no longer valid.

A simple, idealized case for the decoupling of a spherical reservoir is analyzed here. Imagine an infinite elastic body with isotropic far field stress  $\sigma$ . If we remove a sphere from the body, then the stress change at the spherical cavity surface is  $-\sigma$  and therefore the volumetric strain at the boundary of cavity with the infinite body is (Eq. (5))

$$\varepsilon_{v,host} = -\frac{3\sigma}{4G_{host}} \quad (12)$$

If the spherical reservoir, which was removed from the infinite elastic body, is then placed in a stress free environment and cooled by  $\Delta T$ , it would initially undergo expansion due to its removal from the infinite body with a strain equal to  $\varepsilon_v = \sigma/K$ , and simultaneously would contract due to the temperature change with strain equal to  $\varepsilon_v = \alpha_v \Delta T$ . The total volumetric strain on the spherical reservoir is then given by,

$$\varepsilon_{v,res} = \frac{\sigma}{K_{res}} + \alpha_v \Delta T \quad (13)$$

Fig. 2 illustrates the volumetric strains of (a) a stress-free cavity, (b) a stress-free spherical reservoir and (c) their coupled deformation. When an insulated spherical reservoir cools in an infinite body, the volumetric strain induced by the temperature change of the reservoir is governed by Eq. (10) (coupled deformation, Fig. 2(c)). Once the magnitude of the induced volumetric strain becomes greater than the strain of the stress-relieved cavity (Eq. (12)), however, further coupled deformation would induce extensional stresses on both reservoir and cavity wall. Assuming a no-tension criterion on the boundary of the reservoir and the cavity wall, the deformation decouples and may be separated into the distinct deformations of a stress-free cavity (Fig. 2(a)) and a stress-free sphere (Fig. 2(b)).

As illustrated in Fig. 2(d), all three volumetric strain curves (stress free cavity (a), stress free sphere (b) and coupled deformation (c))

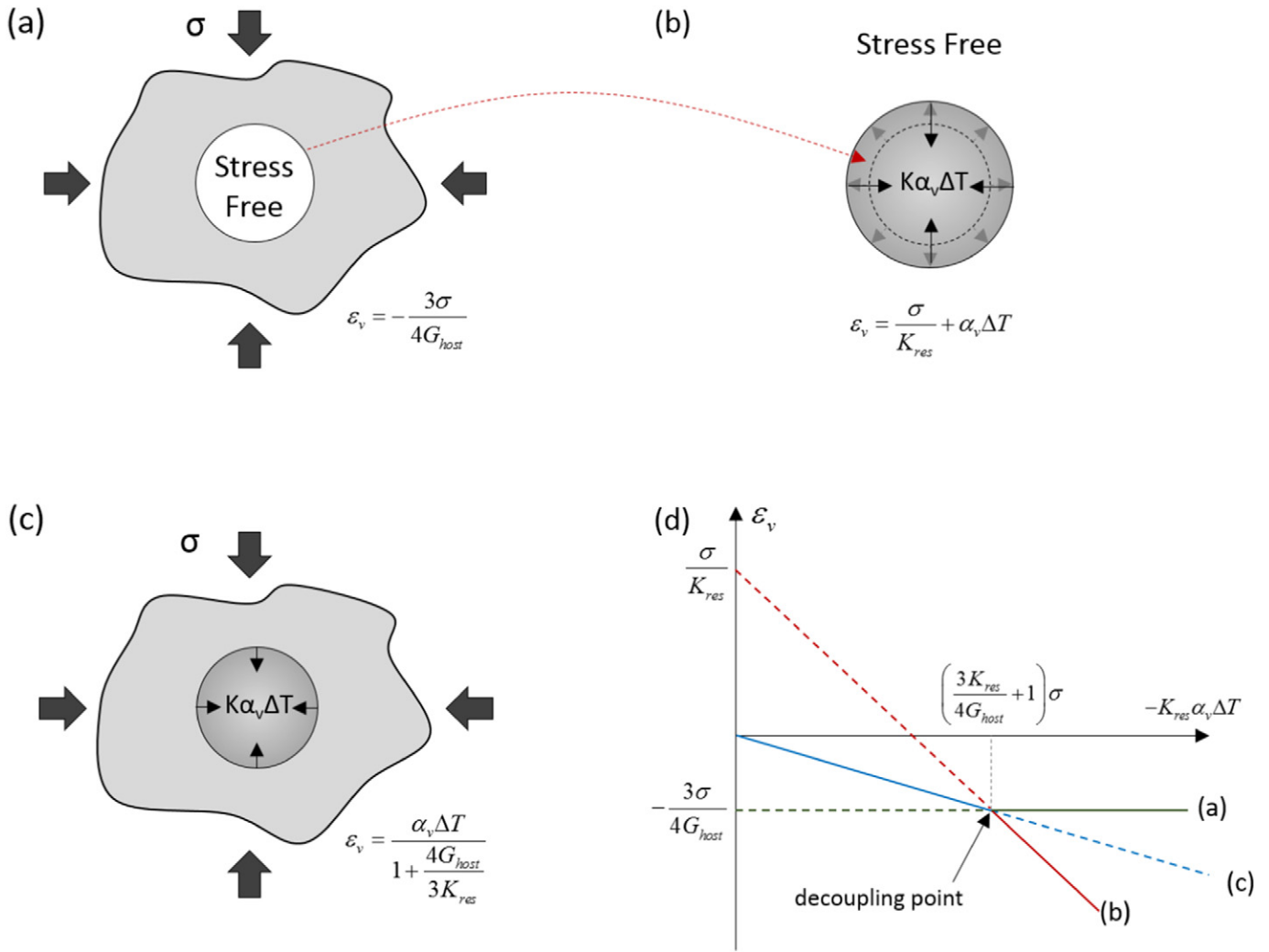


**Fig. 2.** Spherical coupled and decoupled deformations in an infinite body with isotropic far field stress. When a spherical reservoir is removed from a body subjected to an isotropic far field stress  $\sigma$  and the remainder of the cavity is stress free, (a) there will be constant volumetric strain applied to the cavity as  $-3\sigma/4G_{host}$ . If the excluded spherical body is placed in a stress free environment and cooled with a temperature difference  $\Delta T$ , the sphere will have a volumetric strain  $\sigma/K_{res}$  (expansion due to stress removal) plus  $\alpha_v\Delta T$  (thermal expansion/contraction). Case (c) represents the coupled deformation as described in Eq. (10). A volumetric strain vs. thermal stress ( $-K_{res}\alpha_v\Delta T$ ) for all of cases ((a), (b) and (c)) is plotted in (d). The graph shows that all 3 cases intersect at one decoupling point. During the initial stage of falling temperature for a sphere in an infinite body (c), the volumetric strain is defined by coupled deformation (blue solid line); then after the decoupling point, the cavity (a) and the reservoir (b) will be decoupled into two stress free deformations (green solid line for the surrounding rock and the solid red line for the spherical reservoir).

coincide at a single decoupling point. Therefore the decoupling point can be calculated by equating any two of the Eqs. (10), (12) and (13). The volumetric thermal stress at the decoupling point is,

$$K_{res}\alpha_v\Delta T = -\left(\frac{3K_{res}}{4G_{host}} + 1\right)\sigma \quad (14)$$

Rearranging Eq. (14), we obtain the temperature drop to induce decoupling as,

$$\Delta T_{decouple} = -\left(\frac{3K_{res}}{4G_{host}} + 1\right)\frac{\sigma}{K_{res}\alpha_v} \quad (15)$$

Eq. (15) defines the magnitude of temperature drop that induces tensional stress in the reservoir rock. If the reservoir is highly fractured, any further temperature drop will result in opening of the fractures rather than extending the surrounding rocks and the deformation of the rock surrounding the cavity will be significantly reduced – this will result in decreased deformation signal at the surface. The decoupling temperature versus isotropic far field stress is plotted for various bulk moduli in Fig. 3 (assuming  $E_{res} = E_{host}$ ,  $\nu = 0.25$  and  $\alpha_v$

$= 5 \times 10^{-5}$ ). The plot shows the maximum absolute temperature difference for coupled deformation and, as a result, produces the maximum detectable surface deformation. For example, if  $K_{res} = 20$  GPa and the isotropic far field stress is 50 MPa, then the maximum surface deformation would occur when the reservoir rock is cooled to  $\sim 110$  °C. Accordingly, if the rock is cooled by  $> 110$  °C, the measured surface deformation signal will be limited to the threshold temperature change.

### 2.1.3. Permeability change by spherical cooling

It has been shown that the stress applied within the reservoir decreases with thermal contraction and may eventually reach zero (Fig. 2). Thus, such thermal contraction would be expected to result in a concomitant increase in permeability. The following assesses this permeability change using a simple model of isotropic coupled deformation induced by uniform cooling within an embedded spherical reservoir assuming that the fracture is a major fluid conduit (enhanced geothermal system).

The mechanism that induces volume change due to coupled thermo-mechanical unloading (Eq. (10)) may be divided into two different modalities: (i) thermal contraction (assuming constant stress) and (ii) expansion due to stress decrease. Although such

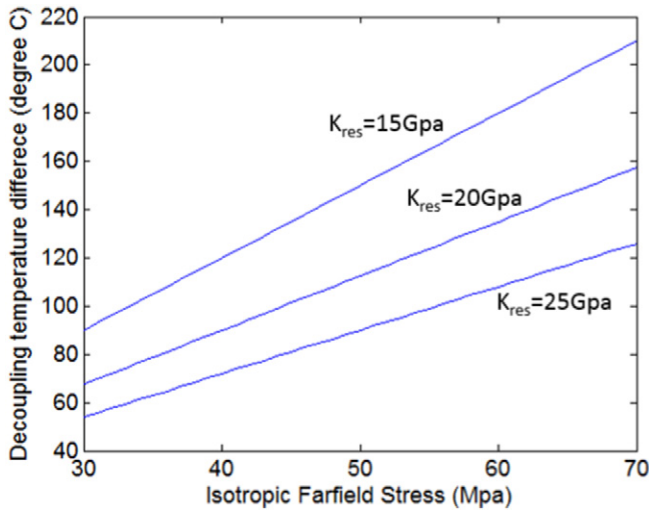


**Fig. 3.** Decoupling temperature vs. isotropic far field stress with various reservoir bulk moduli. The plot assumes  $E_{res} = E_{host}$ ,  $\nu = 0.25$  and  $\alpha_v = 5 \times 10^{-5}$ . The decoupling temperature difference represents the maximum temperature change that can be detected on the surface. For example, in the case of a far field stress of 50 MPa with  $K_{res}$  20 GPa,  $\Delta T \sim 110$  °C induces a maximum surface deformation and further cooling will induce little (or no) additional surface deformation.

mechanisms act concurrently, considering them separately allows us to examine each of the processes and to calculate the magnitude of each effect in terms of the permeability change. We consider a spherical reservoir with equally spaced orthogonal fractures as illustrated in Fig. 4, showing (a) initial state of the reservoir, (b) thermal contraction under constant stress and (c) expansion due to stress decrease. Note that the temperature decrease ((a) → (b)) would contract both rock matrix and pore space together. In contrast, in the process of stress reduction ((b) → (c)), the modulus difference between rock matrix and fracture leads to an unbalanced expansion of the rock matrix and fracture.

The permeability of a rock with a set of parallel fractures with aperture  $b$  and spacing  $S$  can be defined as [Witherspoon et al., 1980, Ouyang and Elsworth, 1993].

$$k = \frac{b^3}{12S} \tag{16}$$

We assume that the fracture is held open by rock bridges of height,  $b$ , that contract with a change in temperature. Induced strain on both fracture and rock matrix due to the temperature change  $\Delta T$  with volumetric thermal expansion coefficient  $\alpha_v$ , in constant stress (Fig. 4 (a) → (b)) are simply  $(\alpha_v \Delta T)/3$ . So aperture changes to  $b(1 + (\alpha_v \Delta T)/3)$  and fracture spacing changes to  $S(1 + (\alpha_v \Delta T)/3)$ . Substituting the result into Eq. (16) yields the permeability due to thermal contraction at constant stress as

$$k_{thermal} = \frac{b^3}{12S} \left(1 + \frac{\alpha_v \Delta T}{3}\right)^2 \tag{17}$$

Permeability decreases only slightly with temperature drop since  $(\alpha_v \Delta T)/3$  is typically in the order of  $10^{-3}$ , the permeability change is not significant.

The second influence is the change in stress that acts within the reservoir. Due to the difference in modulus between fracture and rock matrix, the fracture is strained more than the rock matrix, with this conditioned by the difference in effective modulus of the fracture versus the matrix. This may result in a significant permeability increase (Fig. 4(b) → (c)). A relationship between permeability and strain (as a result of stress change) defines the change in permeability with normal (linear) strain change  $\Delta \epsilon_l$  as modulated by aperture, fracture spacing and modulus reduction ratio  $R_e$  (Ouyang and Elsworth, 1993; Liu et al., 2000) as

$$k_{strain} = \frac{b^3}{12S} \left\{ 1 + \left[ \frac{S}{b} (1 - R_e) + 1 \right] \Delta \epsilon_l \right\}^3 \tag{18}$$

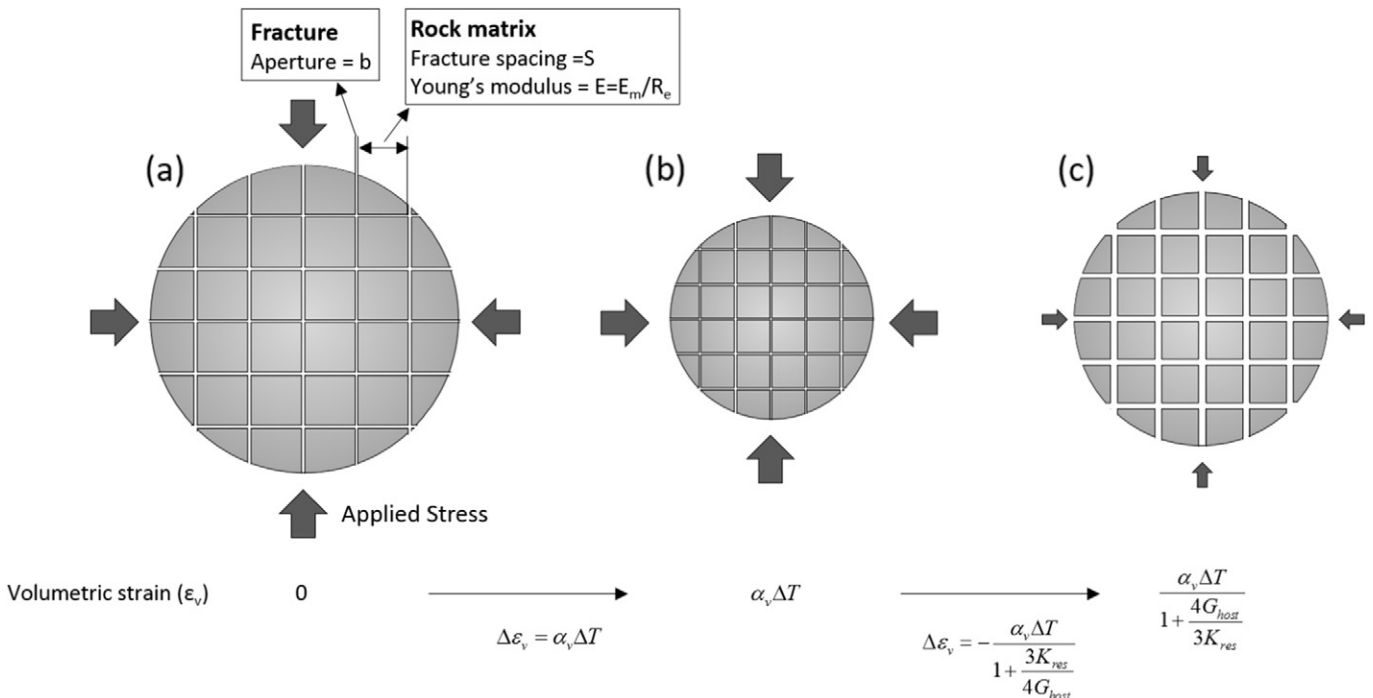


**Fig. 4.** Schematic illustration of two mechanism of volume change due to coupled thermal contraction: (i) thermal contraction (ii) stress reduction. Thermal contraction in constant stress will decrease both aperture and fracture spacing but strain driven by the concomitant reduction in stress results in a net increase in permeability.

The modulus reduction ratio  $R_e$  is defined as.

$$R_e = \frac{E_m}{E} \quad (19)$$

where  $E$  and  $E_m$  are modulus of intact rock and rock mass modulus respectively.

The total volumetric strain induced by thermal contraction within the surrounding rock is derived as Eq. (10). Therefore the strain change due to stress reduction (Fig. 4(b) → (c)) is the difference between the total strain (Eq. (10)) and thermal contraction in constant stress ( $\alpha_v \Delta T$ ), which is,

$$\Delta \varepsilon_v = -\frac{\alpha_v \Delta T}{1 + \frac{3K_{res}}{4G_{host}}} \quad (20)$$

Substituting Eq. (20) into Eq. (18) and assuming isotropic conditions  $\Delta \varepsilon_i = \Delta \varepsilon_v / 3$ , we recover the permeability as.

$$k_{strain} = \frac{b^3}{12S} \left\{ 1 + \left[ \frac{S}{b} (1 - R_e) + 1 \right] \frac{-\alpha_v \Delta T}{3 \left( 1 + \frac{3K_{res}}{4G_{host}} \right)} \right\}^3 \quad (21)$$

Note that  $b^3/12S$  is the original permeability, therefore the parameter in the brackets in Eq. (21) represents the ratio of permeability increase. The permeability increases with a decrease in temperature and its magnitude may be significant, depending on the value of  $S/b$  and  $R_e$ .

Once quenching of the reservoir yields zero stress within the reservoir (reservoir stress decoupling), then further cooling results in an even larger rate of permeability increase with temperature drop. Assuming the boundary between the external host and the reservoir is stationary, aperture increase would be identical to the liner thermal contraction of rock matrix. That gives,

$$\Delta b = -\Delta S = -S \frac{\alpha_v \Delta T}{3} \quad (22)$$

Using this aperture change and ignoring any change in fracture spacing (due to thermal contraction of the blocks of the order of  $\Delta S \sim S \alpha_v \Delta T$ ), permeability will become.

$$k = k_d \left( 1 - \frac{S}{b_d} \frac{\alpha_v \Delta T_d}{3} \right)^3 \quad (23)$$

where,  $k_d$  and  $b_d$  are the permeability and aperture at the temperature of decoupling and  $\Delta T_d$  is temperature change from the decoupling point.

#### 2.1.4. Surface deformation from geothermal operations

The Mogi expressions (Mogi, 1958) for an isotropic spherical pressure source in an elastic half space defines vertical displacement from subsurface volume change  $\Delta V$  as,

$$u_v(r) = \frac{3}{4\pi R^3} z \Delta V \quad (24)$$

where,  $z$  is depth of the source, and  $R^2 = r^2 + z^2$  where  $r$  is horizontal (i.e. radial) distance from the source center. The surface tilt,  $\theta$ , and surface radial strain,  $\varepsilon_r$ , arising from a Mogi source are defined as,

$$\theta(r) = -\frac{9}{4\pi R^5} rz \Delta V \quad (25)$$

and

$$\varepsilon_r = \frac{3}{4\pi R^3} \left( 1 - \frac{3r^2}{R^2} \right) \Delta V \quad (26)$$

Thermal contraction rate induced by heat transfer from the rock to the fluid in a geothermal field is indexed by the heat extraction rate.

Assuming a constant fluid flow rate  $Q_f$  with constant temperature difference between injection and production  $\Delta T_f$ , the rate of heat energy gain of the injected fluid in the reservoir can be expressed as,

$$\dot{H}_f = Q_f \rho_f C_f \Delta T_f \quad (27)$$

Similarly, the heat energy loss from the rock is,

$$\dot{H}_r = V_r \rho_r C_r \dot{T}_r \quad (28)$$

where,  $\rho_f$  and  $\rho_r$  are density of fluid and rock,  $C_f$  and  $C_r$  are heat capacity of the fluid and rock respectively,  $V_r$  is the volume of rock and  $\dot{T}_r$  is the rate of temperature change of the rock.

Equating Eq. (27) and Eq. (28) yields the expression for the rate of temperature change in the reservoir rock as,

$$\dot{T}_r = \frac{Q_f \rho_f C_f}{V_r \rho_r C_r} \Delta T_f \quad (29)$$

Assuming a spherical reservoir, the constrained volumetric strain rate can be recovered by substituting Eq. (29) into Eq. (11).

$$\varepsilon_v = \frac{\dot{V}_r}{V_r} = \frac{1}{1 + \frac{2(1-2\nu)E_{host}}{(1+\nu)E_{res}}} \alpha_v \frac{1}{V_r} \frac{\rho_f C_f}{\rho_r C_r} Q_f \Delta T_f \quad (30)$$

Finally, multiplying by rock volume  $V_r$  in Eq. (30), subsurface volume change rate can be recovered as

$$\dot{V}_r = \frac{1}{1 + \frac{2(1-2\nu)E_{host}}{(1+\nu)E_{res}}} \alpha_v \frac{\rho_f C_f}{\rho_r C_r} Q_f \Delta T_f \quad (31)$$

Substituting Eq. (31) into the Mogi expression (Eq. (24), (25) and (26)), we can obtain surface deformation rates induced by thermal contraction. Note Eq. (31) is maximum estimation since decoupling is not considered here.

Expected maximum surface deformation after 1 year of operation of an geothermal field, assuming  $Q_f = 0.1 \text{ m}^3/\text{s}$ ,  $\alpha = 5 \times 10^{-5}/\text{K}$ ,  $(\rho_f C_f)/(\rho_r C_r) = 2$ ,  $E_{host} = E_{res}$  and Poisson's ratio 0.25 with various geothermal gradients, is presented in Fig. 5. The temperature difference ( $\Delta T_f$ ) is calculated from the geothermal gradient assuming that temperature of the injection fluid and production fluid are identical to ground surface temperature and reservoir temperature, respectively. Deeper source depths yield higher reservoir temperatures and result in a larger volume change. Under these assumptions, the results indicate that the sensitivity of current geodetic tools for tilt and strain ( $\sim 1$  nano-radian and  $\sim 1$  nano-strain, respectively) are generally resolvable for any given source depth, while vertical displacement (for example measured by GPS) is marginal ( $\sim 1$  mm).

The fluid flow rate is  $Q_f = 0.1 \text{ m}^3/\text{s}$  with the assumption of  $\rho_f = 1000 \text{ kg}/\text{m}^3$ ,  $C_f = 4186 \text{ J}/\text{K} \cdot \text{kg}$  and  $\Delta T = 100\text{--}200 \text{ }^\circ\text{C}$ . This yields a total energy production rate of 42 to 84 MW. Using a plant efficiency of 12% (Zarrouk and Moon, 2014) this represents 5–10 MW of geothermal power production. We show that this 5–10 MW operation can yield mm/year scale subsidence rates at a reservoir depth of 2000 m. Accordingly, during much larger geothermal operations ( $\sim 100$  MW scale), typically observed cm/year scale subsidence is expected. Our result shows that surface deformation may largely result from thermal contraction.

A simple one-dimensional model for describing thermal drawdown and consequent volume change patterns in geothermal reservoirs is explored in Fig. 6. The model compares two end-members of thermal drawdown behavior: (i) the case where a sharp thermal front transits the reservoir (Fig. 6(a) red) and (ii) the case where uniform thermal drawdown occurs (i.e., thermal front absent case, Fig. 6(a) blue). The model describes a reservoir  $1000 \text{ m} \times 200 \text{ m} \times 200 \text{ m}$  at a depth of

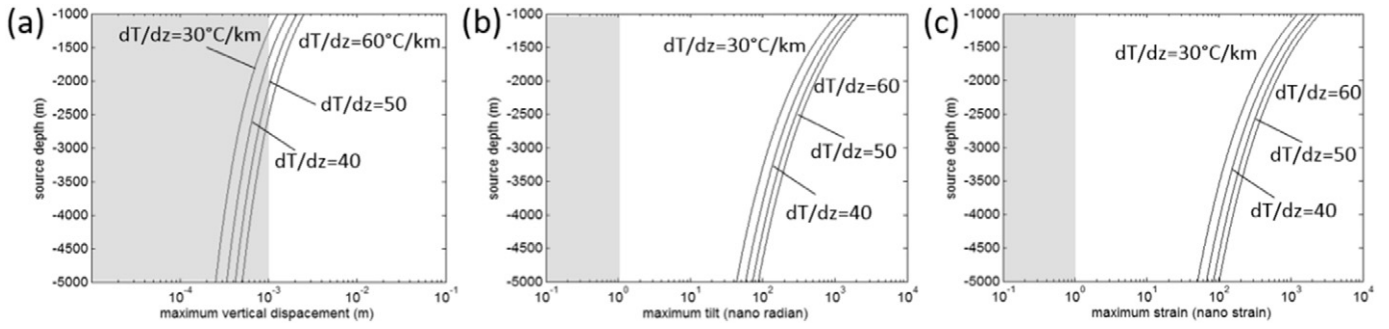


**Fig. 5.** Maximum surface deformations vs. source depth with various geothermal gradients. (a) Vertical displacement, (b) surface tilt and (c) radial strain. Assumed parameters are,  $Q_f = 0.1 \text{ m}^3/\text{s}$ ,  $\alpha = 5 \times 10^{-5}/\text{K}$ ,  $E_{res} = E_{host}$ , Poisson's ratio 0.25 and 1 year of thermal production (~5–10 MW plant scale). Gray area in the panels denotes undetectable deformation (1 nano-radian and 1 nano-strain).

2500 m with reservoir properties of volumetric thermal expansion coefficient  $\alpha = 5 \times 10^{-5}$ ,  $E_{res} = E_{host}$  and Poisson's ratio 0.25. Cold water ( $\Delta T = -100 \text{ }^\circ\text{C}$ ) is injected at one end of the reservoir and produced at the other. The reservoir is divided into 10 equal-sized zones with equivalent Mogi sources located at the center of each. The resulting surface deformation is determined by the activated superposed Mogi solutions from each source. Where the thermal front is present, the temperature decreases by  $100 \text{ }^\circ\text{C}$  only at selected zones near the injector. For the

uniform thermal depletion model, the temperature change and resulting strain is distributed uniformly between all zones. (Fig. 6(a)).

The resulting surface deformation signals of vertical displacement, tilt and strain with three different depletion states (10%, 30% and 50% depleted) are shown in Fig. 6. The red curves denote the case for the sharp thermal front and blue curves denote the case of uniform depletion with maximum, minimum and zero values marked by circles. The maximum, minimum and zero values migrate for the thermal front but are stationary

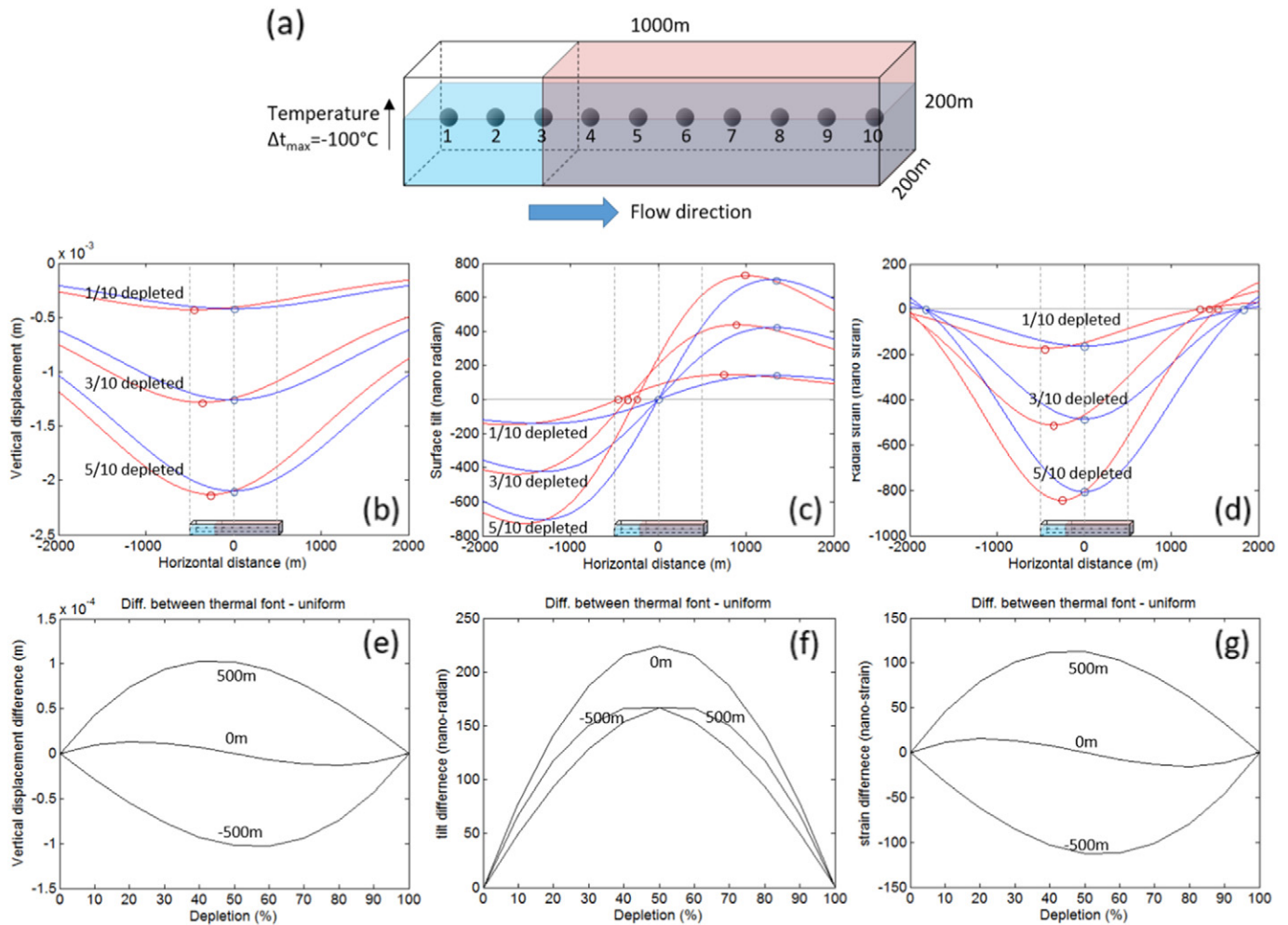


**Fig. 6.** Surface geodetic signals of thermal front present (red) and absent (blue) case.  $1000 \text{ m} \times 200 \text{ m} \times 200 \text{ m}$  size reservoir is placed at a depth of 2500 m. The reservoir is divided by 10 equal sized zone and surface deformations are calculated by superposed Mogi solutions. Plots (b), (c) and (d) represent the geodetic signals on the surface and plots (e), (f) and (g) represent the difference of geodetic signals between the two cases at certain surface locations (injection point, middle of the reservoir and production point). It is clear that the difference in the thermal drawdown behavior can be identified with currently available tilt and strain meters.

for uniform depletion. Fig. 6(e), (f) and (g) represent the differences in deformation magnitudes at the injection point ( $-500$  m), the middle of the reservoir ( $0$  m) and at the production location ( $500$  m) for the contrasting cases of plug- and uniform-depletion. The two end member responses to depletion can be clearly identified by the magnitude of tilt (maximum difference  $\sim 230$  nano-radians) and strain (maximum difference  $\sim 110$  nano-strains) although not with vertical displacement (maximum difference  $\sim 0.1$  mm). This simple model shows that the magnitude of surface deformation, and its variation, is sufficient to identify the reservoir depletion behavior and therefore specific geodetic tools could be used for reservoir imaging of thermal depletion.

## 2.2. Shear deformation

We discussed above the mechanical processes of thermal contraction and unloading and argue that the magnitude of strain and stress change is significantly large in a typical geothermal reservoir. Isotropic thermal unloading induced by spherical cooling will significantly reduce normal stress on a fault while shear stress is maintained (see Fig. 7 Mohr circle) – and may trigger reactivation. Gan and Elsworth (2014) discuss this thermally driven slow reactivation process in a 2D geothermal system.

A number of seismic events, some of significant magnitude ( $M > 3$ ), occur simultaneous with fluid circulation in geothermal reservoirs (Majer et al., 2007). Monitoring the shear offset of such faulting using surface or near-surface geodetic tools could potentially allow for visualization of the evolving major flow paths within the geothermal reservoir, and thus an analysis of the mechanical processes related to fluid injection-induced seismicity. Although it is widely observed that slip induces surface deformation, it often receives less attention as a source of surface deformation in a geothermal field because the energy released by a single seismic event is insufficient to induce the observed long-term surface deformation (typically several centimeter of subsidence per year). For example, the Okada model indicates that the maximum deformation induced by the largest micro-seismicity at the Newberry project (fault surface area  $62,500$  m<sup>2</sup> with  $2.3$  mm slip at depth  $2500$  m (Fang et al., 2015)) would yield a vertical displacement of  $0.006$  mm and surface tilt of  $3.5$  nano-radians, respectively, of which only the tilt signal is marginally resolvable with current instruments.

When describing fault reactivation by fluid injection, however, it is inappropriate to consider each individual seismic event independently; rather, cumulative displacement may be recovered from repeating events on the same fault or from slip that occurs aseismically. For instance, the shear offset observed across one borehole at Soultz geothermal experiment (the upper Rhine graben in Alsace, France) was significantly larger than the expected slip calculated from the contributing individual seismic events (Cornet et al., 1997). In addition, observations of injection induced shear slip offset are typically far larger than the slip calculated from induced seismicity (Guglielmi et al., 2015a, 2015b). These observations might be explained by two mechanisms: (i) stacking of seismic fault events within a fault zone and (ii) aseismic or slow-slip fault reactivation. The first mechanism has often been observed and simulated in the development of injection-induced

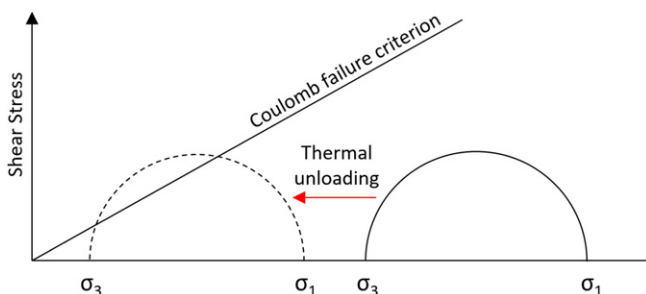


Fig. 7. Mechanism of fault reactivation in isotropic thermal unloading (spherical cooling).

seismicity (Horton, 2012; McClure and Horne, 2013; Gischig, 2015), while the second mechanism is reviewed and discussed for tectonic plate boundary slip (Peng and Gomberg, 2010) and with injection triggered fault slip (Zoback et al., 2012; Guglielmi et al., 2015a and Guglielmi et al., 2015b).

Another interesting observation of direct slip measurements by Guglielmi et al. (2015a, 2015b) is that the slip front (fracture tip) is always ahead of the fluid-pressurized front. Similar behavior is observed in numerical simulations of induced slip (Gischig, 2015). The slip front should be evaluated from the force balance of the slip driving stress (induced by effective normal stress reduction) within the pressure (and/or thermal) front and the resisting stress (friction) between pressure front and slip front. Thus the slip front in fault reactivation is always ahead of the pressure (and/or thermal) front and the size and magnitude of slip is strongly dependent on the orientation and frictional properties of the slipping fault. This behavior shows that a larger slip zone can be generated by a smaller area of stress perturbation increasing the likelihood of a large event.

The Okada model assumes a slip source within a finite rectangular fault with uniform displacement embedded within an elastic half-space (Okada, 1985). Fig. 8 shows the fault geometry used for the Okada model. With the geometry at depth  $D$ , and of width  $W$  and length  $L$  fault centered at the origin, the Okada expression for surface deformation at  $(x,y,0)$  is,

$$F(x,y,0) = f\left(x + \frac{L}{2}, p + \frac{W}{2}\right) - f\left(x + \frac{L}{2}, p - \frac{W}{2}\right) - f\left(x - \frac{L}{2}, p + \frac{W}{2}\right) + f\left(x - \frac{L}{2}, p - \frac{W}{2}\right) \quad (32)$$

where,  $F$  results (integrated over the fault surface) in surface deformation,  $p = y \cos \delta + D \sin \delta$  and  $f(\xi, \eta)$  is a formula that has different expressions for each of displacement, tilt and strain and also in the directions  $x$  and  $y$  (here  $\xi$  and  $\eta$  are notations used in the Okada equations and  $\eta$  is not the power plant efficiency in Table 1, see Okada, 1985).

Fig. 9 shows the relationships between fault size and maximum magnitude of surface deformations at an optimal surface location calculated from an Okada solution assuming a rectangular fault at a depth  $2500$  m with a  $60^\circ$  dip. It indicates that the magnitude of surface deformation increases with both fault size and shear offset. In fact, the fault size and slip distance are mutually dependent. Assuming constant stress drop across the fault, the larger the area of the fault, the larger the shear offset (Zoback and Gorelick, 2012). Accordingly, it is expected that a

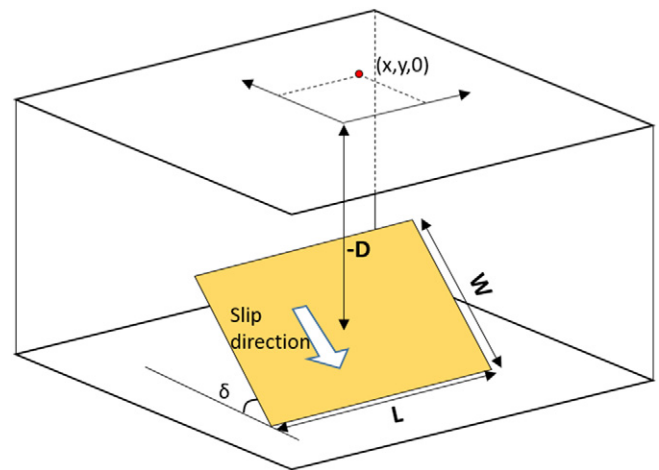


Fig. 8. Fault geometry used for the Okada model with the yellow rectangle representing a slip surface with a dip angle of  $\delta$ , horizontal length of  $L$ , width (along slip direction) of  $W$  and depth  $D$ .

**Table 1**  
Nomenclature

Symbol	Unit	Quantity	Symbol	Unit	Quantity
$\epsilon_v$	–	Volumetric strain	$\alpha_v$	/K	Volumetric thermal expansion coefficient
$\Delta T$	K	Temperature change	$\Delta P$	Pa	Pressure change
$E$	Pa	Young's modulus	$k_n$	Pa/m	Fracture normal stiffness
$G$	Pa	Shear modulus	$S$	m	Fracture spacing
$K$	Pa	Bulk modulus	$\sigma$	Pa	Normal stress
$b$	m	Fracture aperture	$R_e$	–	Modulus reduction ratio
$u_v$	m	Vertical displacement	$\theta$	rad	Surface tilt
$r$	m	Surface radial distance	$z$	m	Source depth (Mogi)
$\dot{H}_f$	J/s	Fluid energy change rate	$\dot{H}_r$	J/s	Rock energy change rate
$\rho_f$	kg/m <sup>3</sup>	Fluid density	$\rho_r$	kg/m <sup>3</sup>	Rock density
$C_f$	J/K·kg	Fluid specific heat	$C_r$	J/K·kg	Rock specific heat
$\Delta T_f$	K	Temperature difference of fluid	$\dot{T}_r$	K/s	Rate of temperature change of rock
$Q_f$	m <sup>3</sup> /s	Volumetric fluid flow rate	$L$	m	Fault length
$W$	m	Fault width	$\delta$	rad	Fault dip angle
$D$	m	Fault depth	$\eta$	–	Geothermal plant efficiency
$W_p$	J/s	Electrical power			

sizable area of fault slip would generate detectable surface deformation signals. The Okada slip solution (Fig. 9) indicates that for a 200 m × 200 m fault at depth 2500 m, even several millimeters of slip can be detected with tilt- and strain-meters.

2.3. Summary and comparison of surface deformation

Maximum surface deformation calculated by the Mogi and Okada models, with fixed source geometry  $W = 500$ ,  $L = 1000$  and  $\delta = 60^\circ$  (Fig. 8) and with various volume changes and shear offsets, are shown in Fig. 10. The gray area represents signals that are undetectable with current geodetic techniques (~1 mm vertical displacement, ~1 nano-radian and ~1 nano-strain). The equivalent heat production period is specified in parenthesis in the plots (a1), (a2) and (a3) assuming coupled spherical deformation with  $Q_f = 0.1$  m<sup>3</sup>/s,  $\alpha = 5 \times 10^{-5}$ /K,  $(\rho_f C_f)/(\rho_r C_r) = 2$ ,  $E_{host} = E_{res}$ ,  $\nu = 0.25$  and  $\Delta T = -100$  °C. Also the equivalent moment magnitude with a shear modulus 15 GPa is noted in parentheses in the plots (b1), (b2) and (b3). In all cases, a detailed deconvolution of subsurface deformation can be achieved by tilt and strain but not generally through measurement of vertical displacements. For example, a volume change of 10<sup>3</sup> m<sup>3</sup> (20 days of geothermal operation) is not resolvable by vertical displacement for any source depth deeper than 1000 m, while it remains resolvable in both tilt and strain. Similarly, 1 mm to 1 cm of slip is undetectable in vertical displacement, but it easily detectable with tilt and strain.

Since both volume change and slip induces surface deformation concurrently, it is necessary to distinguish the causal mechanism from observed surface deformation. One indication of different of mechanisms would be a timing of the events. In general, it is presumed that shear

slip events would be episodic and staccato, while the volume change signal due to energy extraction would be more continuous and gradual. In addition, dilatation and slip may be further distinguished by their surface deformation patterns – slip induces a more spatially compact and asymmetric form of surface deformation.

Fig. 11 represents a comparison of the shape profiles induced by slip (red) and volume change (blue). Three different vertical displacement profiles (from the volume changes at two depths of 1400 m and 2500 m and from slip at a depth 2500 m) are plotted in Fig. 11(a). For comparison, the magnitude of all three deformations are fixed to have the same maximum vertical displacement at the surface. The figure clearly shows that the shear events (red solid line) yield more intense and asymmetric surface deformation than the deformation induced by volume change at the same depth (blue solid line). The ratio of maximum vertical displacement and tilt of the Mogi volume solution and Okada slip solution are plotted in Fig. 11(c), which further emphasizes the difference in surface deformation arising from these distinct mechanisms.

3. Field data and discussion

Surface deformations have been observed at a variety of geothermal reservoirs using near-surface tilt and surface displacements measured by InSAR. Tilt measurement data are available for two reservoirs in Japan, namely, the Hijiori injection test site and the Okuaizu geothermal field (Vasco et al., 2002a). In addition, InSAR vertical displacements are available from various geothermal fields: Brady Hot Springs, Coso, Dixie Valley, East Mesa, Heber, Salton Sea, San Emidio (Ali et al., 2016; Eneva et al., 2012; Falorni et al., 2011;

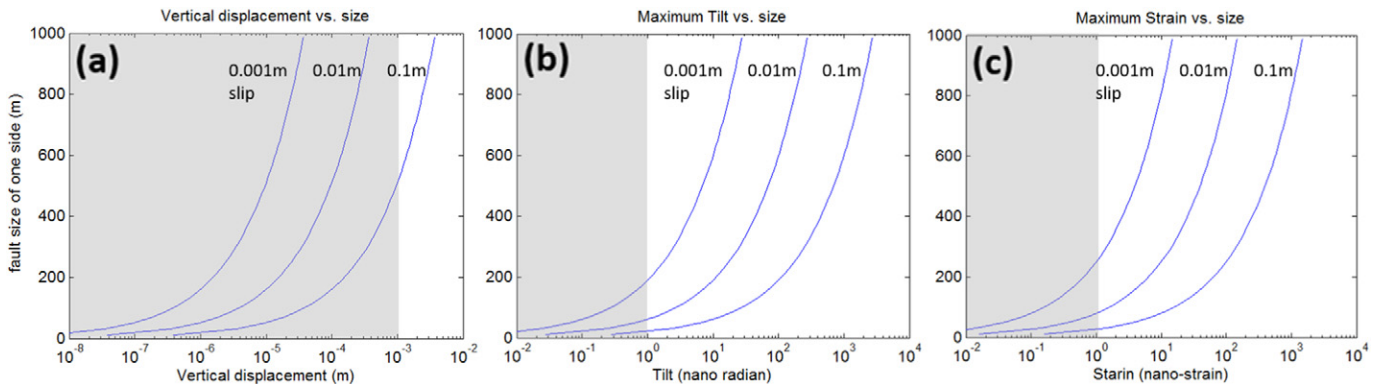


**Fig. 9.** Maximum magnitude of surface deformation vs. fault size (length of one side of rectangular fault) with three slip distances (0.001 m, 0.01 m and 0.1 m) at depth 2500 m. The magnitude of surface deformation increase with both fault area and total slip. The gray areas in each plot show the nominal sensitivity of each measurement type from current state-of-the-art instruments.

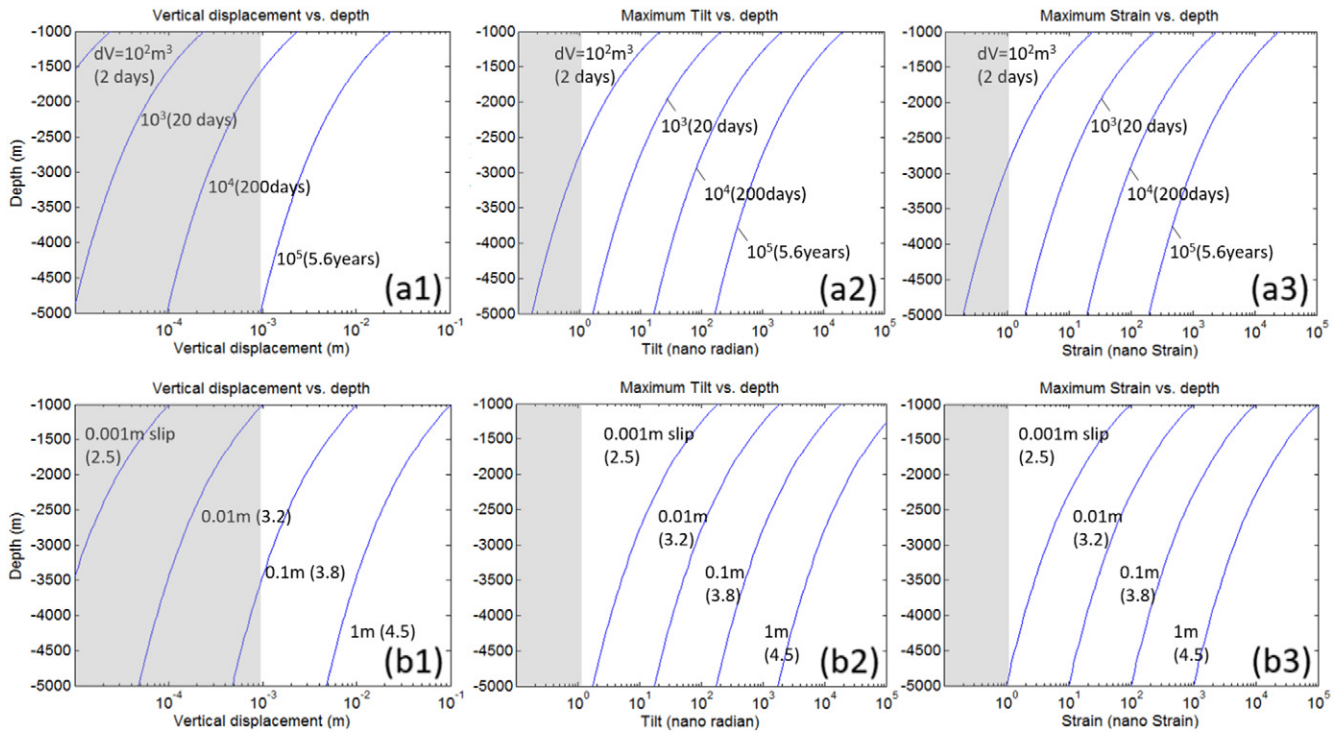


**Fig. 10.** Log-linear plot of maximum surface deformations induced by various contractile volume changes and by shear slip. (a1): maximum vertical displacement from contractile volume change. (b1) maximum vertical displacement from shear slip. (a2): maximum tilt from contractile volume change. (b2) maximum tilt from shear slip. (a3): maximum radial strain from contractile volume change. (b3) maximum horizontal strain from shear slip. Geometry assumed for the slip solution is  $W = 500$  m,  $L = 1000$  m and  $\theta = 60^\circ$  shown in Fig. 8. The gray areas in each plot show the nominal sensitivity of each measurement type from current state-of-the-art instruments.

Fialko and Simons, 2000; Foxall and Vasco, 2003; Vasco et al., 2002b; Vasco et al., 2013). The advantages of tilt observations over InSAR-inferred displacement measurements are the low detection limit (high sensitivity) and dense temporal sampling, which allows one to recover a detailed record of short-term behavior. InSAR methods, in contrast, have a higher detection limit (lower sensitivity) for imaging subsurface deformation as deduced from vertical

displacement (Fig. 10), but long term stability, relatively low cost of InSAR data and processing and its ability to produce synoptic surface deformation images makes this technique attractive and therefore widely used.

The magnitude of thermal contraction in geothermal fields can be estimated from energy extraction rate. With a conversion efficiency of  $\eta$  (from thermal recovery to electrical conversion, including running at

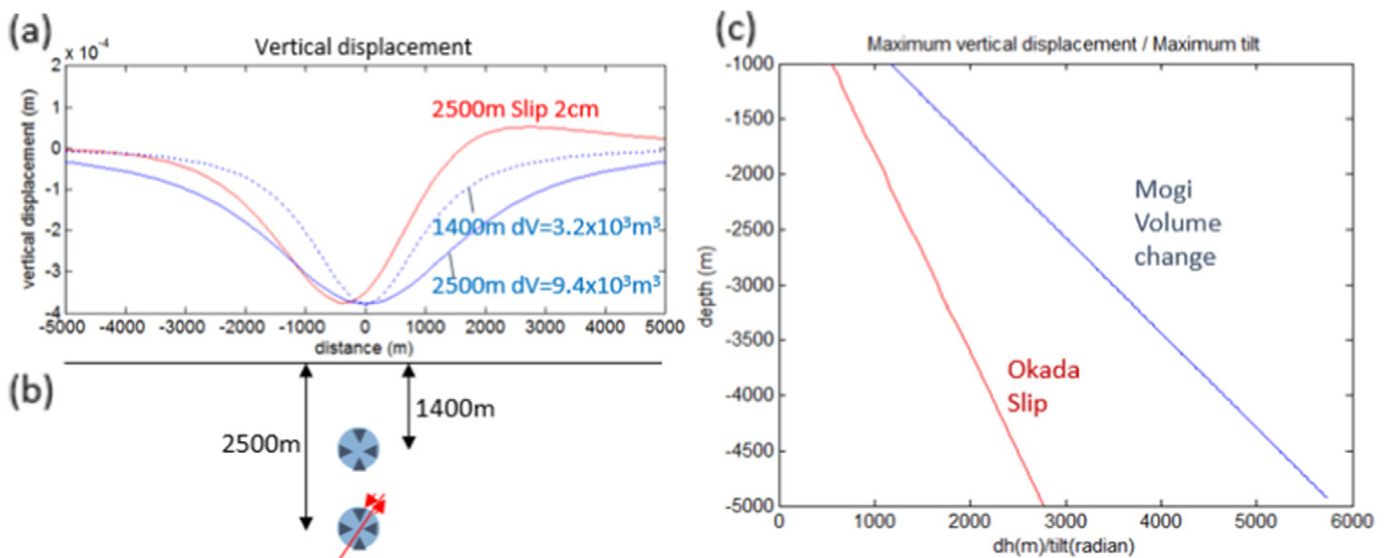


**Fig. 11.** (a): Vertical displacement profile induced by (b) Mogi and Okada slip sources. Red profile in (a) is Okada slip solution of 2 cm slip at depth 2500 m with fault geometry same as Fig. 9. Blue lines denotes Mogi volume change solution at depth 2500 m (solid line) and 1400 m (dashed line). For comparison, all source magnitudes are fixed to yield the same maximum surface displacement. Figure (c) plots of maximum vertical displacement divided by maximum tilt vs. depth. It shows that the ratio of maximum vertical displacement and maximum tilt for a Mogi source is  $\sim 2\times$  that of the Okada slip dislocation.

sub-capacity) and net electricity produced from a geothermal power plant  $W_p$ , the rate of heat energy loss of reservoir rock can be calculated as.

$$\dot{H}_r = \frac{W_p}{\eta} \quad (33)$$

The average conversion efficiency  $\eta$  in geothermal plants is ~12% (Zarrouk and Moon, 2014). Using this, 1 year of operation of a geothermal field with  $W_p = 10$  MW yields  $\sim 2.6 \times 10^{15}$  J of net energy recovery from the subsurface reservoir rock.

Combining Eqs. (11), (28), (33) and  $\varepsilon_v = \dot{V}_r/V_r$  yields the rate of subsurface thermal volume change as,

$$\dot{V}_r = \frac{1}{1 + \frac{2(1-2\nu)E_{host}}{(1+\nu)E_{res}}} \alpha_v \frac{W_p}{\eta \rho_r C_r} \quad (34)$$

Using  $\eta = 12\%$  and assuming typical rock properties of  $\alpha_v = 5 \times 10^{-5}$ ,  $\rho_r = 2700$  kg/m<sup>3</sup>,  $C_r = 900$  J/kg·K,  $E_{host} = E_{res}$  and  $\nu = 0.25$ , 1 year of operation of a 10 MW geothermal plant yields  $\sim 3.0 \times 10^4$  m<sup>3</sup> of subsurface volume reduction. As discussed in Section 2.1.4, this magnitude is sufficiently large to be detected. Assuming a point source (Mogi model) the volume change at 2000 m depth can induce ~1.7 mm of vertical displacement, ~800 nano-radians of tilt and 900 nano-strains of contraction.

Assuming single Mogi point source (Eq. (34)), surface subsidence rate driven by thermal contraction in an existing geothermal field can be estimated. Fig. 12(a) shows the calculated surface subsidence rate with full (up to current capacity) plant operation (red filled circles) and satellite-observed surface deformation (blue filled circles) for seven different geothermal fields. Note that we used 2014 plant capacity since we could not find actual electricity generation magnitudes over the observed period. The resulting deformation calculations, however, scale geothermal operations to observed surface deformations, and thus can be used to infer the approximate contribution of thermal contraction. Fig. 12(b) shows two direct tilt observations in Japan and expected tilt magnitudes during the observations of a 300 m<sup>3</sup> (water) injection test for Hijiori and 30 days of geothermal operations for Okuaizu. Detailed inputs and references for both plots are listed in Table 2.

Fig. 12(a) shows that magnitudes of observed surface deformations (red) are comparable to calculated surface subsidence rate (blue) showing that ~cm/year subsidence rates are expected due to thermal contraction. A higher subsidence rate is generally observed in larger scale geothermal fields, with the one noted exception of Dixie Valley. This

similarity in magnitude implies that thermal contraction plays a significant role in inducing the large observed surface deformations. We note that these expected surface deformations are somewhat overestimated because (i) we use current (2014) maximum operational capacity, which may be larger than the actual electricity generation over the same period, (ii) only a single Mogi source is modeled for each example, and (iii) decoupling of the spherical reservoir from the elastic crust is not considered. Accordingly, the result of smaller surface deformation observations than predicted in the San Emidio, Heber, Salton Sea and Coso geothermal fields are easily explicable. The calculations for East Mesa and Dixie Valley, however, suggest that observed subsidence cannot be explained by thermal contraction only. Slow and continuous pressure drawdown in shallow strata is often suggested as possible cause (Vasco et al., 2002b; Foxall and Vasco, 2003; Ali et al., 2016). We do not reject that such processes can generate measurable surface deformation. Rather, we argue here that thermally driven slow fault reactivation, which has been ignored previously, also induces significant surface deformation and must be considered as one potential major cause.

Fig. 12(b) compares tiltmeter observations to expected magnitudes (Mogi model) through the operational period of the Hijiori geothermal injection test and at the Okuaizu geothermal field in Japan. Similar to Fig. 12(a), expected surface deformation is denoted by red filled circles and observations are denoted in blue. Both tiltmeter experiments show very large magnitudes (> micro-radian) of tilt. These magnitude of tilt (Mogi model) require  $10^5$ – $10^6$  m<sup>3</sup> of subsurface volume change which are unlikely to be a result from pressurization or thermal contraction for the short observation periods. We suspect that the large deformations are driven by systematic fault reactivation in shear. Inversion of the surface tilt (Vasco et al., 2002a) to obtain subsurface volume shows that the source has a strong geometric relevance to existing faults.

Several observations of surface deformation have strong apparent geometric relevance to existing faults. Surface deformation at the Brady Hot Springs and San Emidio geothermal fields, which are located within steeply dipping fault zones, develop parallel to existing faults (Ali et al., 2016; Eneva et al., 2011). Similarly, surface subsidence of the Dixie Valley field, bounded by two major faults (Foxall and Vasco, 2003), is manifest as a rapid subsurface expression of its graben structure. Furthermore, the San Emidio (Falorni et al., 2011) and Heber (Eneva et al., 2012) fields show largely asymmetric surface deformation with associated significant uplift, which can be an attributed to steeply dipping (~90°) slow fault reactivation,

We further note that the inversion of surface deformation observations to constrain subsurface volume changes often requires a shallow

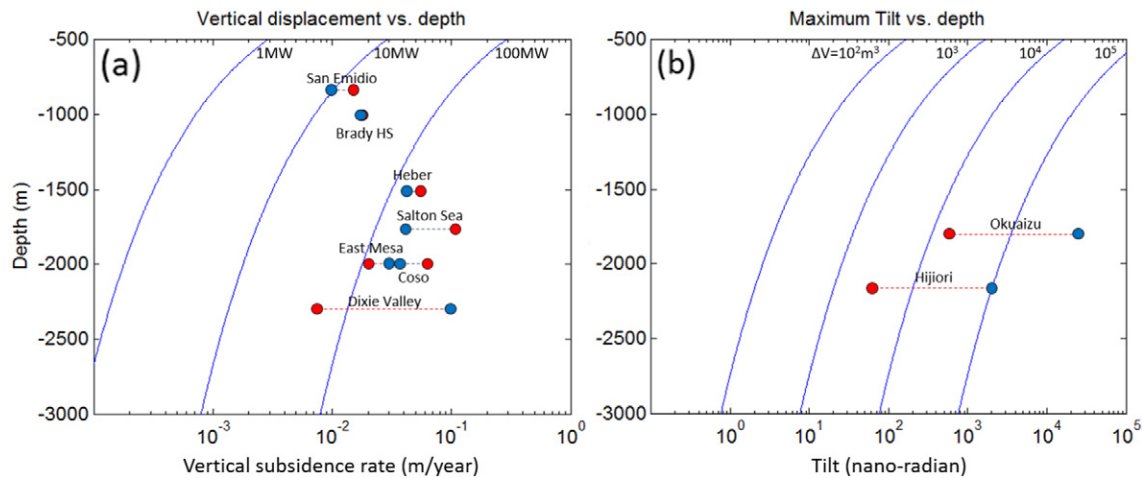


**Fig. 12.** Comparison of modeled maximum surface deformation driven by thermal contraction (red filled circles) and observed maximum deformation (blue filled circles). East Mesa, Dixie Valley, Hijiori and Okuaizu field exhibit larger observed magnitudes than maximum expected displacements from the Mogi model. This implies the possible involvement of shear offset in producing the large observed surface deformation.

**Table 2**  
Summary data of analyzed geothermal fields defining surface deformation, plant capacity and average reservoir depths.

InSAR vertical displacement					
Field name	Observation year	Subsidence rate	Reference	2014 capacity <sup>a,b</sup>	Average depth <sup>b</sup>
Brady Hot Springs	2013–2014	16 mm/yr	Ali et al., 2016	26 MW	988 m
San Emidio	2005–2010	10 mm/yr	Eneva et al., 2011	14 MW	823 m
Salton Sea	2006–2008	40 mm/yr	Eneva et al., 2012	437 MW	1750 m
Heber	2003–2010	42 mm/yr	Eneva et al., 2012	180 MW	1500 m
East Mesa	1992–1994	29 mm/yr	Eneva et al., 2012	115 MW	2000 m
Coso	1993–1999	35 mm/yr	Fialko and Simons, 2000	300 MW	2000 m
Dixie Valley	1996–1997	100 mm/yr	Foxall and Vasco, 2003	62 MW	2298 m
Tilt Response					
Field name	Observation duration	Observed tilt	Reference	Volume change	Average depth
Okuaizu	30 days	>30 $\mu$ rad	Vasco et al., 2002a	20,000m <sup>c</sup>	1800 m
Hijiori (injection)	2 days	~2 $\mu$ rad	Vasco et al., 2002a	300m <sup>d</sup>	2150 m

<sup>a</sup> 2014 Annual U.S. & Global Geothermal Power Production Report.

<sup>b</sup> Open energy information. (<http://en.openei.org>).

<sup>c</sup> 65 MW current capacity with 30 days observation.

<sup>d</sup> Injection during the tilt observation.

depth for the deformation source; for example, this is the case for Hijiori, Okuaizu, Brady Hot Springs and Dixie Valley (Vasco et al., 2002a; Ali et al., 2016; Foxall and Vasco, 2003). In actuality, slip on finite planar faults may also explain the observation of a shallow source – dislocation slip on planar faults produces more intense surface deformation than volume changes from a shallower spherical source (Fig. 11), and fluid-pressure-induced fault reactivation is favored at shallow depths (Fang et al., 2015) due to the lithostatic stress profiles within the upper crust.

#### 4. Summary and conclusion

We have reviewed and modeled surface deformation induced by cold-water injection in geothermal reservoirs through constrained isotropic volume change and injection-induced shear offset. To understand subsurface thermal process, we first define mechanical processes of subsurface deformation as a result of the cooling of a spherical fractured reservoir in an infinite medium. Our model defines the relations between thermal contraction, stress change and permeability evolution. Using parameters of typical geothermal environments, the model suggests two major mechanisms capable of inducing large surface deformations, viz.: (i) thermal contraction and (ii) slow fault reactivation. We assess surface deformations (vertical displacement, tilt and strain) induced by the two mechanisms using Mogi (point source contraction) and Okada (shear slip) models and compare their magnitudes with the sensitivities (~1 nano-radian and ~1 nano-strain) of current high precision surface geodetic instruments.

Thermal contraction induced by the operation for one year of a 10 MW capacity plant with plant efficiency 12% (Zarrouk and Moon, 2014) can yield a subsurface volume change of  $\sim 3.0 \times 10^4 \text{ m}^3$ . Assuming a Mogi point source at a depth of 2000 m, this generates a maximum of ~1.7 mm surface subsidence, ~800 nano-radians of surface tilt and ~900 nano-strains of surface strain. The result represents typically observed magnitudes of surface subsidence (cm/year) in much larger geothermal operations (>100 MW), suggesting that the observed surface deformation may be largely driven by thermal contraction. These observed and calculated magnitudes also demonstrate that reservoir depletion can be monitored with high precision geodetic measurements. For example, 10 days of field operations of a 10 MW capacity geothermal field can induce surface deformations of >20 nano-radian and >20 nano-strain from thermal contraction, alone. This magnitude is well above current instrumental detection limits.

Stress changes recovered from such spherical inclusion models suggest that magnitudes of thermal unloading in geothermal reservoirs can be highly significant and can trigger slow fault reactivation. The Okada

slip dislocation model shows that surface deformations induced by fault reactivation are also of sufficient magnitude to be detected and monitored by surface geodesy. For example, a 1 mm slip offset on a 1000 m  $\times$  500 m fault dipping at 60° at a center-depth of 2000 m will induce surface signals of >20 nano-radian and >20 nano-strain signals – also well above instrumental detection limits.

Significant surface deformations have been observed around active geothermal sites both with tiltmeters and with InSAR. Considering heat production rates and sizes of putative subsurface faults, the observed large surface deformation is likely contributed by the combined influence of both thermal contraction and slip offset. Although the two mechanisms may act concurrently to produce surface deformation, their respective influence may be deconvolved from the temporal and spatial variation of the surface deformation. High precision surface geodetic measurements combined with long term stable InSAR monitoring have a high potential to successfully image geothermal reservoirs, which in turn may be useful in understanding the evolution of their permeability structure, thermal depletion and fault reactivation, and ultimately in optimally managing production.

#### Acknowledgement

This work is a partial result of support provided by DOE Grant DE-EE0006761. This support is gratefully acknowledged.

#### References

- Ali, S.T., Akerley, J., Baluyut, E.C., Cardiff, M., Davatzes, N.C., Feigl, K.L., Foxall, W., Fratta, D., Mellors, R.J., Spielman, P., Wang, H.F., Zemach, E., 2016. Time-series analysis of surface deformation at Brady Hot Springs geothermal field (Nevada) using interferometric synthetic aperture radar. *Geothermics* 61:114–120. <http://dx.doi.org/10.1016/j.geothermics.2016.01.008>.
- Cooper, H.W., Simmons, G., 1977. The effect of cracks on the thermal expansion of rocks. *Earth Planet. Sci. Lett.* 36, 404–412.
- Cornet, F.H., Helm, J., Poitrenaud, H., Etchecopar, A., 1997. Seismic and aseismic slips induced by large-scale fluid injections. *Pure Appl. Geophys.* 150:563–583. <http://dx.doi.org/10.1007/s000240050093>.
- Eneva, M., Falorni, G., Teplow, W., Morgan, J., Rhodes, G., Adams, D., 2011. Surface deformation at the San Emidio geothermal field, Nevada, from satellite radar interferometry. *GRC Trans.* 35, 1647–1653.
- Eneva, M., Adams, D., Falorni, G., Morgan, J., 2012. Surface deformation in Imperial Valley, CA, from satellite radar interferometry. *GRC Trans.* 36, 1339–1344.
- Eshelby, J., 1957. The determination of the elastic field of an ellipsoidal inclusion, and related problems. *Proc. R. Soc. London, Ser. A* 214, 376–396.
- Falorni, G., Morgan, J., Eneva, M., 2011. Advanced InSAR techniques for geothermal exploration and production. *GRC Trans.* 35.
- Fang, Y., den Hartog, S.A.M., Elsworth, D., Marone, C., Cladouhos, T., 2015. Anomalous distribution of microearthquakes in the Newberry Geothermal Reservoir: mechanisms and implications. *Geothermics* <http://dx.doi.org/10.1016/j.geothermics.2015.04.005>.

- Fialko, Y., Simons, M., 2000. Deformation and seismicity in the Coso geothermal area, Inyo County, California: Observations and modeling using satellite radar interferometry. *J. Geophys. Res.* 105:21781. <http://dx.doi.org/10.1029/2000JB900169>.
- Foxall, B., Vasco, D., 2003. Inversion of synthetic aperture radar interferograms for sources of production-related subsidence at the Dixie Valley geothermal field. *Proceedings: Twenty-eighth Workshop on Geothermal Reservoir Engineering Stanford University, Stanford, California, January 27–29*.
- Gan, Q., Elsworth, D., 2014. Analysis of fluid injection-induced fault reactivation and seismic slip in geothermal reservoirs. *J. Geophys. Res. Solid Earth*:3340–3353 <http://dx.doi.org/10.1002/2013JB010679>.
- Geothermal Energy Association, 2014. *2014 Annual U.S. & Global Geothermal Power Production Report*.
- Gischig, V.S., 2015. Rupture propagation behavior and the largest possible earthquake induced by fluid injection into deep reservoirs. *Geophys. Res. Lett.*:7420–7428 <http://dx.doi.org/10.1002/2015GL065072>.
- Gladwin, M.T., 1984. High precision multicomponent borehole deformation monitoring. *Rev. Sci. Instrum.* 55.
- Goodman, R., 1980. *Introduction to Rock Mechanics*. John Wiley & Sons.
- Guglielmi, Y., Cappa, F., Avouac, J., Henry, P., Elsworth, D., 2015a. Seismicity triggered by fluid injection – induced aseismic slip. *Science* 348, 1224–1226.
- Guglielmi, Y., Elsworth, D., Cappa, F., Henry, P., Gout, C., Dick, P., Durand, J., 2015b. In situ observations on the coupling between hydraulic diffusivity and displacements during fault reactivation in shales. *J. Geophys. Res. Solid Earth*:1–23 <http://dx.doi.org/10.1002/2014JB011237>.
- Horton, S., 2012. Disposal of hydrofracturing waste fluid by injection into subsurface aquifers triggers earthquake swarm in Central Arkansas with potential for damaging earthquake. *Seismol. Res. Lett.* 83:250–260. <http://dx.doi.org/10.1785/gssrl.83.2.250>.
- Liu, J., Elsworth, D., Brady, B.H., Muhlhaus, H.B., 2000. Strain-dependent fluid flow defined through rock mass classification schemes. *Rock Mech. Rock. Eng.* 33, 75–92.
- Majer, E.L., Baria, R., Stark, M., Oates, S., Bommer, J., Smith, B., Asanuma, H., 2007. Induced seismicity associated with enhanced geothermal systems. *Geothermics* 36:185–222. <http://dx.doi.org/10.1016/j.geothermics.2007.03.003>.
- McClure, M.W., Horne, R.N., 2013. *Discrete Fracture Network Modeling of Hydraulic Stimulation*. Springer.
- Mogi, K., 1958. Relations between the eruptions of various volcanoes and the deformations of the ground surface around them. *Bull. Earthq. Res. Inst., Univ. Tokyo* 36, 99–134.
- Okada, Y., 1985. Surface deformation due to shear and tensile faults in a half-space. *Bull. Seismol. Soc. Am.* 75:1135–1154. [http://dx.doi.org/10.1016/0148-9062\(86\)90674-1](http://dx.doi.org/10.1016/0148-9062(86)90674-1).
- Ouyang, Z., Elsworth, D., 1993. Evaluation of groundwater flow into mined panels. *Int. J. Rock Mech. Min. Sci. Geomech.* 71–79.
- Peng, Z., Gombert, J., 2010. An integrated perspective of the continuum between earthquakes and slow-slip phenomena. *Nat. Geosci.* 3:599–607. <http://dx.doi.org/10.1038/ngeo940>.
- Vasco, D.W., Karasaki, K., Nakagome, O., 2002a. Monitoring production using surface deformation: the Hijiori test site and the Okuaizu geothermal field, Japan. *Geothermics* 31:303–342. [http://dx.doi.org/10.1016/S0375-6505\(01\)00036-0](http://dx.doi.org/10.1016/S0375-6505(01)00036-0).
- Vasco, D., Wicks, C., Karasaki, K., Marques, O., 2002b. Geodetic Imaging: reservoir monitoring using satellite interferometry. *Geophys. J. Int.* 149:555–571. <http://dx.doi.org/10.1046/j.1365-246X.2002.01569.x>.
- Vasco, D.W., Rutqvist, J., Ferretti, A., Rucci, A., Bellotti, F., Dobson, P., Oldenburg, C., Garcia, J., Walters, M., Hartline, C., 2013. Monitoring deformation at the Geysers geothermal field, California using C-band and X-band interferometric synthetic aperture radar. *Geophys. Res. Lett.* 40:2567–2572. <http://dx.doi.org/10.1002/grl.50314>.
- Witherspoon, P., Wang, J., Iwai, K., Gale, J., 1980. Validity of cubic law for fluid flow in a deformable rock fracture. *Water Resour. Res.* 16, 1016–1024.
- Wright, C.A., Davis, E.J., Minner, W.A., Ward, J.F., Weijers, L., Schell, E.J., Hunter, S.P., 1998. Surface tiltmeter fracture mapping reaches new depths - 10,000 beyond? *Soc. Pet. Eng.* 39919. <http://dx.doi.org/10.2118/39919-MS>.
- Yu, H.S., Houlby, G.T., 1991. Finite cavity expansion in dilatant soils: loading analysis. *Geotechnique* 41:173–183. <http://dx.doi.org/10.1680/geot.1991.41.2.173>.
- Zarrouk, S.J., Moon, H., 2014. Geothermics efficiency of geothermal power plants: a worldwide review. *Geothermics* 51:142–153. <http://dx.doi.org/10.1016/j.geothermics.2013.11.001>.
- Zoback, M.D., Gorelick, S.M., 2012. Earthquake triggering and large-scale geologic storage of carbon dioxide. *Proc. Natl. Acad. Sci.* 109:10164–10168. <http://dx.doi.org/10.1073/pnas.1202473109>.
- Zoback, M.D., Kohli, A., Das, I., McClure, M., 2012. The importance of slow slip on faults during hydraulic fracturing stimulation of shale gas reservoirs. *Soc. Pet. Eng.* 155476. <http://dx.doi.org/10.2118/155476-MS> (p. SPE).